Designing Highly Conductive Sodium-Based Metal Hydride Nanocomposites: Interplay between Hydride and Oxide Properties

Laura M. de Kort, Oscar E. Brandt Corstius, Valerio Gulino, Andrei Gurinov, Marc Baldus, and Peter Ngene*

Sodium-based complex hydrides have recently gained interest as electrolytes for all-solid-state batteries due to their light weight and high electrochemical stability. Although their room temperature conductivities are not sufficiently high for battery application, nanocomposite formation with metal oxides has emerged as a promising approach to enhance the ionic conductivity of complex hydrides. This enhancement is generally attributed to the formation of a space charge layer at the hydride-oxide interface. However, in this study it is found that the conductivity enhancement results from interface reactions between the metal hydride and the oxide. Highly conductive $NaBH_4$ and $NaNH_2$/oxide nanocomposites are obtained by optimizing the interface reaction, which strongly depends on the interplay between the surface chemistry of the oxides and the reactivity of the metal hydrides. Notably, for $NaBH_4$, the best performance is obtained with Al_2O_3, while $NaNH_2/SiO_2$ is the most conductive $NaNH_2$/oxide nanocomposite with conductivities of, respectively, 4.7×10^{-5} and 2.1×10^{-5} S cm^{-1} at 80 °C. Detailed structural characterization reveals that this disparity originates from the formation of different tertiary interfacial compounds, and is not only a space charge effect. These results provide useful insights for the preparation of highly conductive nanocomposite electrolytes by optimizing interface interactions.

1. Introduction

The advancement in portable electronics coupled with the desire to reduce our carbon footprint through renewable energy utilization has led to an ongoing search for excellent energy storage technologies. Currently, rechargeable lithium-ion batteries are one of the most widely used energy storage systems, with applications ranging from mobile devices to electric vehicles.[1,2] However, due to increasing performance demands, lithium-ion batteries are challenged by safety concerns inherent to their flammable organic liquid electrolytes as well as the rising cost of raw materials.[3] Consequently, many research efforts are directed toward the development of batteries beyond current lithium-ion technology.

Sodium-ion batteries are a particularly promising alternative to the conventional Li-ion battery. They have mainly attracted interest for large scale applications due to the high abundance, accessibility, and hence low cost of sodium.[4–8] Analogous to Li-ion batteries, Na-ion batteries can be operated with solutions of an ion conducting salt in an organic solvent as the electrolyte. However, these liquid electrolytes are volatile and unstable in contact with high energy density electrodes. Solid-state electrolytes (SSEs) are often safer and in many cases compatible with high energy density electrodes. For example, the solid-state Na-ion conductor β-Al_2O_3 can be combined with a metallic Na anode (specific capacity = 1165 mAh g^{-1}) as well as a sulfur cathode (specific capacity = 1672 mAh g^{-1}).[9,10] Therefore, forming an all-solid-state battery (ASSB), in which the liquid electrolyte is replaced by a solid electrolyte, could improve device safety as well as storage capacity.[11,12] Consequently, the development of all-solid-state sodium-ion batteries could lead to safer and affordable energy storage devices.

Solid-state Na-ion conductors with high ionic conductivity at ambient temperature as well as good electrochemical stability and electrode compatibility are crucial for the implementation of Na-ion ASSBs operating at room temperature. Interestingly, solids that can conduct sodium ions have been investigated even before the creation of the lithium-ion battery. As early as 1967, fast 2D Na-ion transport has been observed in β-Al_2O_3,[13] which was followed by the introduction of 3D ion conducting NASICON (Na Super Ionic Conductor) in 1976.[14–16] In recent years, more classes of Na-ion conductors

L. M. de Kort, O. E. Brandt Corstius, V. Gulino, P. Ngene
Materials Chemistry and Catalysis
Debye Institute for Nanomaterials Science
Utrecht University
Universiteitweg 99, 3584 CG Utrecht, The Netherlands
E-mail: p.ngene@uu.nl
A. Gurinov, M. Baldus
NMR Spectroscopy
Bijvoet Center for Biomolecular Research
Utrecht University
Padualaan 8, 3584 CH Utrecht, The Netherlands

**ADVANCED
SCIENCE NEWS**

www.advancedsciencenews.com

**ADVANCED
FUNCTIONAL
MATERIALS**

www.afm-journal.de

have been studied, including oxides, sulfides, thiophosphates, and complex hydrides, each with their own advantages and disadvantages.[17,18] To illustrate, sulfide- and thiophosphate electrolytes display excellent ionic conductivities at ambient temperature, but their chemical stability is poor.[17–19] Oxide-based ion conductors, on the other hand, have a higher (electro) chemical stability, but their manufacturing process is often expensive and their interfacial contact with the electrode is poor.[10,18] While research has largely focused on the development of suitable oxide- and sulfide-type SSEs, complex hydrides have recently emerged as interesting alternative. This class of materials displays several unique properties that could be beneficial for ASSBs compared to oxide- and sulfide-type ion conductors.

Complex metal hydrides are solids with an ionic lattice composed of metal cations, e.g., Li^+, Na^+, or Mg^{2+}, and metal hydride anions, such as $[BH_4]^-$, $[NH_2]^-$, $[B_{10}H_{10}]^{2-}$, and $[CB_{11}H_{12}]^-$. Research in their potential as solid ion conductors was initiated by the discovery of fast lithium-ion mobility (10^{-3} S cm^{-1}) in $LiBH_4$ after a reversible phase change from orthorhombic to hexagonal phase at 108 °C.[20] Thereafter, similar structural transitions to highly conductive phases have been discovered for other complex hydrides as well, including $Na_2B_{10}H_{10}$ (10^{-2} S cm^{-1} at 110 °C),[21] $NaCB_{11}H_{12}$ (10^{-1} S cm^{-1} at 110 °C),[22] and even $Mg(BH_4)_2$ xNH_3 (10^{-3} S cm^{-1} at 55 °C).[23] In addition to high ionic conductivity, other benefits of complex hydrides are their low density and relatively high electrochemical stability (e.g., ≈4 V for $NaCB_{11}H_{12}$),[24] as well as the ability to form stable electrolyte-electrode interfaces.[25–29] These properties make complex hydrides uniquely interesting for novel all-solid-state sodium-ion batteries. However, for successful incorporation of metal hydride SSEs in ASSBs, sufficient ionic conductivity (10^{-3} S cm^{-1}) at room temperature is a prerequisite. Therefore, the development of strategies that enhances conductivity in complex hydrides at ambient temperature is of major importance.

Several promising strategies to enhance ion mobility in metal hydrides at ambient temperature are being explored, namely partial ionic substitution, nano structuring, and nanocomposite formation. For both lithium- as well as sodium-based complex hydrides, it has been established that partial substitution of the complex hydride anion by different anions (e.g., Cl^-, Br^-, I^-, $[NH_2]^-$, $[B_{10}H_{10}]^{2-}$) results in the formation of phases that are highly conductive at RT.[26,30,31] Additionally, the conductivity of complex metal hydrides can be greatly enhanced via nano structuring with a mechanochemical treatment[32] or via nanocomposite formation, by intimately mixing the metal hydride with a high surface area non-conducting oxide scaffold, such as SiO_2 or Al_2O_3.[33–42] For the latter, the enhancement in ionic conductivity is attributed to the formation of a highly conductive layer at the interface between the ion-conducting salt and the insulating scaffold.[40,43] As a consequence, the chemical nature of the metal oxide has a large effect on the ionic conductivity. For example, Choi et al. showed that the conductivity of $LiBH_4/Al_2O_3$ is twice as high as that of $LiBH_4/SiO_2$ nanocomposites prepared in the same way.[44] Interestingly, while the space charge model, i.e., a local ion redistribution, is often used to explain the formation of this conductive layer,[45–47] the exact nature of the interface layer and the interface interactions remain unclear. Notably several $LiBH_4$/oxide nanocomposites have been successfully implemented in ASSBs operating at intermediate temperatures.[34,39,48] For instance, Gulino et al. recently reported on an ASSB working at room temperature using $LiBH_4/MgO$ composite as the SSE.[48] Overall, it has clearly been demonstrated that nanocomposite formation is a useful strategy to increase Li-ion conductivity in metal hydride SSEs.

Despite the clear evidence for conductivity enhancement in $LiBH_4$/oxide nanocomposites, studies on Na-based metal hydrides, such as $NaBH_4$, $NaCB_{11}H_{12}$ and $NaNH_2$, are scarce. To the best of our knowledge, the effect of nanocomposite formation on the Na^+ mobility in $NaBH_4$ has only been explored in two recent studies by Luo et al. and Dou et al.[49,50] In the former study, it was shown that confinement of $NaBH_4$ in a mesoporous SiO_2 scaffold leads to a limited improvement in ionic conductivity of one order of magnitude.[49] On the other hand, Dou et al. reported that a slightly larger conductivity increase to 5.8×10^{-8} S cm^{-1} at room temperature using MgAl-layered double hydroxides as the scaffold.[50] The latter study demonstrates that the ionic conductivity of $NaBH_4$-based nanocomposites differs greatly depending on the surface chemistry of the scaffold material; however, the conductivity enhancement has remained rather small.[41,42] The same is true for $NaCB_{11}H_{12}/SiO_2$ nanocomposites, where a 30-fold conductivity improvement from 1×10^{-5} S cm^{-1} up to 3×10^{-4} S cm^{-1} is observed.[51]

Understanding the conductivity enhancement mechanism, e.g., a space charge layer or interface reaction, is crucial to obtain nanocomposites with high Na-ion conductivity. However, so far little is known about the exact interactions at metal hydride-oxide interface. In this work, we investigate the impact of nanocomposite formation on the Na-ion conductivity in complex hydrides in detail. In particular, we study how the ionic conductivity is affected by the chemical nature of the oxide scaffold by incorporating SiO_2 and Al_2O_3, two widely used high surface area oxides with large differences in surface chemistry, wettability, and chemical reactivity. Using nanocomposites based on $NaBH_4$ or $NaNH_2$ and these metal oxides as model systems, we found that the conductivity enhancement results from interfacial reactions leading to different interfacial compounds. The interface reactions depend strongly on the interplay between the properties of the metal hydride and the oxide scaffold material. Based on this understanding, we achieved about three orders of magnitude increase in the ionic conductivities of the nanocomposites by using the appropriate metal oxide scaffold. Specifically, conductivities of 4.7×10^{-5} and 2.1×10^{-5} S cm^{-1} at 80 °C are obtained for $NaBH_4$ and $NaNH_2$, respectively, which are higher than previously reported in literature. Interestingly, while γ-Al_2O_3 results in the highest conductivity in case of $NaBH_4$, the highest conductivity for the $NaNH_2$/oxide nanocomposites was obtained with SiO_2. Results from electrochemical impedance spectroscopy (EIS), DRIFTS, and solid-state NMR measurements indicate that the difference in conductivity is due to the strength of the interaction between the hydrides and the oxide, which is influenced by the stability of the metal hydride and the ability to wet the oxide surface.

2209122 (2 of 15)

2. Results and Discussion

### 2.1. Structural Differences between NaBH₄- and NaNH₂/Oxide Nanocomposites

The structural properties of the synthesized $NaBH_4$/oxide and $NaNH_2$/oxide nanocomposites with a pore filling fraction of 130% have been investigated. To start, the effect of the melt infiltration synthesis and the incorporation of the metal hydrides in the pores of the mesoporous scaffolds is discussed based on the chemical and structural changes revealed by DRIFTS, DSC, XRD, and N_2 physisorption measurements.

In **Figure 1**a, the DRIFTS absorbance spectra of the $NaBH_4$/Al_2O_3 and $NaBH_4$/SiO_2 nanocomposites, as well as pure $NaBH_4$, Al_2O_3 and SiO_2 are shown. In the spectra, the characteristic vibrations of macrocrystalline $NaBH_4$ can be observed by bands between 2500 and 2000 cm^{-1}, corresponding to $[BH_4^-]$ stretching vibrations,[57,58] and bands between 3200 and 3600 cm^{-1}.[59] These characteristic bands are present in the DRIFTS spectra of both $NaBH_4$/Al_2O_3 and $NaBH_4$/SiO_2 nanocomposites as well. In previous studies on nanoconfined $LiBH_4$, a broadening of these peaks was seen, which was attributed to an increase in the rotational freedom of $[BH_4^-]$ induced by nanocomposite formation.[43] For the $NaBH_4$ nanocomposites, this effect is less evident, though slightly broader peaks are observed for the $NaBH_4$/Al_2O_3 nanocomposite.
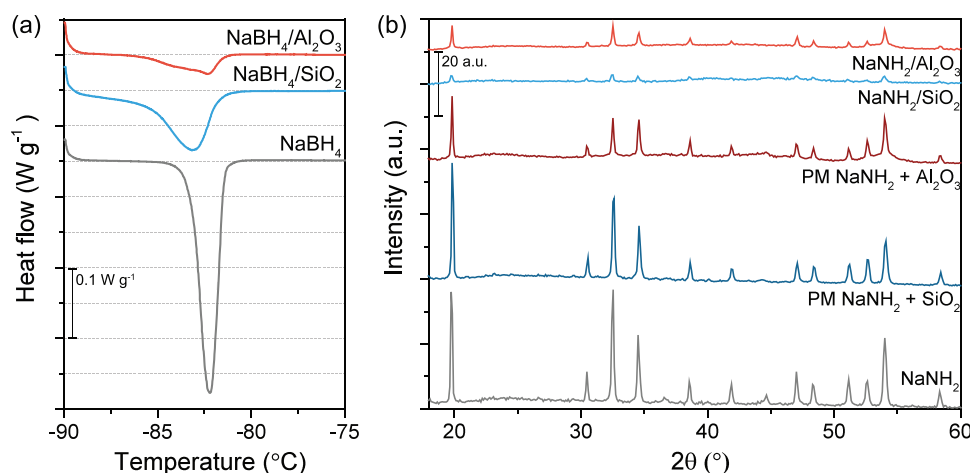
The second region of interest corresponds to the hydroxyl stretching vibrations in Al_2O_3 and SiO_2 appearing between 3850 and 3000 cm^{-1}.[60] For Al_2O_3, several broad bands related to vibrations of linear and bridged hydroxyl groups are seen in the region between 3800 and 3000 cm^{-1}. In the SiO_2 spectrum, a sharp absorption peak is present at 3747 cm^{-1}, which is ascribed to isolated and geminal silanol groups, or "free" silanols. Additionally, a broad band that represents hydrogen bound (vicinal) silanol groups and physiosorbed water is observed between 3700 and 3000 cm^{-1}. Notably, after melt infiltration the vibrations assigned to surface hydroxyl groups are no longer visible in the spectra of both $NaBH_4$/Al_2O_3 and $NaBH_4$/SiO_2. Generally, this is associated with a reaction or interactions between the −[OH] group and the confined electrolyte, thereby suppressing the hydroxyl vibration.[42,43] This indicates that $NaBH_4$ covers the surface of the mesoporous oxides, and that an interaction or reaction occurs at the $NaBH_4$ – metal oxide interface.

In the same way as for $NaBH_4$/oxide nanocomposites, DRIFTS analysis was used to study the structural properties of $NaNH_2$/Al_2O_3 and $NaNH_2$/SiO_2 nanocomposites. The DRIFTS spectra of the nanocomposites and pristine compounds are displayed in Figure 1b. In the spectra of both nanocomposites vibrations, that are characteristic for $NaNH_2$ are observed between 3800 and 2800 cm^{-1}.[61,62] Especially the sharp vibrations at 3260 and 3210 cm^{-1} attributed to $[NH_2^-]$ stretching vibrations display clear changes compared to pristine $NaNH_2$. Similar to $LiBH_4$- and $NaBH_4$/oxide nanocomposites, the peaks have become less intense and slightly broader after melt infiltration, especially for the $NaNH_2$/SiO_2 nanocomposite. Moreover, in both nanocomposite spectra two bands are seen at 2060 and 1970 cm^{-1} that are less pronounced in pure $NaNH_2$. To investigate the origin of these features, the DRIFTS spectrum of pure $NaNH_2$ subjected to the same heat treatment as the nanocomposites, i.e., 30 min at 225 °C, was collected (Figure S2, Supporting Information). It is observed that this spectrum displays the same features, confirming that these peaks are not the result of nanocomposite formation, but rather an irreversible structural change in $NaNH_2$ after heating to 225 °C. Finally, in the spectra of the $NaNH_2$/oxide nanocomposites the vibrations related to the metal oxide hydroxyl groups between 3700 and 3000 cm^{-1} are no longer present. Again this can be assigned to interfacial interactions or reactions between the sodium salt and the −[OH] groups on the Al_2O_3 and SiO_2 surface.[43] This indicates that the used synthesis conditions result in interaction of $NaNH_2$ with the oxide surface, comparable to the results on $NaBH_4$.

The incorporation of $NaBH_4$ in the pores of the mesoporous scaffolds was studied further with differential scanning calorimetry (DSC), X-ray diffraction (XRD), and N_2 physisorption. The DSC curves of $NaBH_4$/SiO_2 and $NaBH_4$/Al_2O_3 nanocomposites as well as pure $NaBH_4$ are presented in **Figure 2**a. In the DSC curve of pure $NaBH_4$, the phase transition from tetragonal P4₂/nmc (LT phase) to cubic F_m-3m (HT phase) $NaBH_4$ is observed by an endothermic peak starting at -83 °C.[63,64] Using integration of the peak area, it was possible to verify that the enthalpy of this phase transition is 23.5 J g^{-1} (or 0.89 kJ mol^{-1}) in accordance with literature.[64,65] Similarly, in the DSC curves of both $NaBH_4$/oxide nanocomposites, a broad endothermic peak with an onset of −85 °C is seen, which is related to macrocrystalline $NaBH_4$. Note that a peak corresponding to the presence
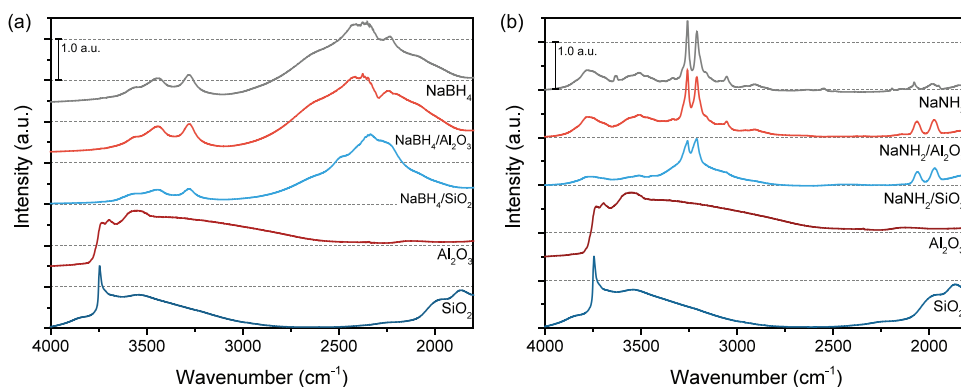
Figure 1. DRIFTS spectra of a) $NaBH_4$/oxide and b) $NaBH_2$/oxide nanocomposites with 130% pore filling fraction displaying the regions related to hydroxyl stretching vibrations, as well as characteristic $[BH_4]^-$ and $[NH_2]^-$ vibrations.

**ADVANCED
SCIENCE NEWS**

www.advancedsciencenews.com

**ADVANCED
FUNCTIONAL
MATERIALS**

www.afm-journal.de

Figure 2. a) DSC graphs of macrocrystalline NaBH$_4$ and NaBH$_4$/oxide nanocomposites with 130% pore filling fraction. b) XRD diffraction patterns of NaNH$_2$/oxide physical mixtures (PM) and corresponding nanocomposites. The diffraction pattern of NaNH$_2$ is shown for comparison.

of nanoconfined NaBH$_4$ was not observed. As the phase transition in nanoconfined materials is known to occur at lower temperatures than for macrocrystalline materials, this suggests that the nanoconfined NaBH$_4$ undergoes the phase transition at temperatures below −90 °C[66] which is the limit of the DSC apparatus.

Using the peak area of the macrocrystalline NaBH$_4$ peak and the enthalpy of the phase transition, it is possible to calculate the fractions of nanoconfined (intraporous) and macrocrystalline (extraporous) NaBH$_4$ in the nanocomposites.[67] The results are summarized in **Table 1**. This approach shows that in the NaBH$_4$/Al$_2$O$_3$ nanocomposite the pores are completely filled with NaBH$_4$. As a result, 79% of the total amount of NaBH$_4$ is confined inside the scaffold pores and 21% is present as extraporous NaBH$_4$, as required to ensure sufficient Na$^+$ conduction over the non-conducting oxide particles. On the other hand, for the NaBH$_4$/SiO$_2$ nanocomposite it was found that only 35% of NaBH$_4$ has been incorporated in the SiO$_2$ pores, while 65% remained outside of the scaffold. This corresponds to a pore filling of only 46%, significantly lower than intended. This clearly demonstrates that melt infiltration has resulted in the complete infiltration of NaBH$_4$ in the pores of Al$_2$O$_3$, whereas only partial incorporation occurs in the SiO$_2$ scaffold.

These results are further corroborated by XRD analysis (Figure S3a, Supporting Information), which shows a large decrease in the long-range crystallinity of NaBH$_4$ when it is melt infiltrated in Al$_2$O$_3$, whereas long-range crystallinity is mostly preserved for NaBH$_4$/SiO$_2$. Nanoconfined materials typically lack long-range crystallinity, due to the nanosized

crystallites that form in the small scaffold pores, which means that long-range crystallinity in metal hydride nanocomposites is often associated with extraporous (non-confined) material.[67] Similar differences were observed in the physisorption curves of NaBH$_4$/Al$_2$O$_3$ and NaBH$_4$/SiO$_2$ nanocomposites with different pore filling fractions, as shown in Figure S3 (Supporting Information). Upon introduction of a small volume of NaBH$_4$ (15% of the scaffold pore volume) in the nanocomposite, the large BET surface area and pore volume that is characteristic for this SiO$_2$ scaffold is almost completely lost. This demonstrates that the small amount of NaBH$_4$ cover the outer surface of the scaffold and blocks the pores rather than infiltrate them. In contrast, the gradual reduction of the BET surface area and pore volume of the Al$_2$O$_3$ upon introduction of increasing amounts of NaBH$_4$ (15%, 30%, and 130% of the scaffold pore volume), demonstrates that the metal hydride readily infiltrates the γ-Al$_2$O$_3$ scaffold.

The distinct difference in NaBH$_4$ infiltration in the different scaffolds can be explained by the physical principles governing melt infiltration. In general, pores of a certain scaffold can be filled spontaneously by a liquid (or molten solid) when capillary forces draw the liquid or molten phase inside the scaffold pores. This phenomenon occurs when the liquid readily spreads over, or 'wets', the surface of the solid. Whether a liquid wets a surface depends on the surface energy of the solid γ_{sv}, the surface tension of the liquid γ_{lv} and the solid–liquid interface energy γ_{sl}. Based on Young's equation (Equation 1), it can be determined if a system "wetting" or "non-wetting".

$$\cos\theta = \frac{\gamma_{sv} - \gamma_{sl}}{\gamma_{lv}} \tag{1}$$

A contact angle $\theta < 90°$ corresponds to wetting, while a system is non-wetting if $\theta > 90°$.[67] By comparing the surface energies of SiO$_2$ and Al$_2$O$_3$, it becomes clear that the surface energy for SiO$_2$ (0.26 J m^{-2}) is significantly lower than that of Al$_2$O$_3$ (1.52 J m^{-2}).[68,69] Therefore, it is more difficult for NaBH$_4$ to infiltrate the pores of SiO$_2$ and consequently only partial NaBH$_4$ incorporation is observed for NaBH$_4$/SiO$_2$, while complete infiltration is achieved for the NaBH$_4$/Al$_2$O$_3$

Table 1. Differential Scanning Calorimetry results of the NaBH$_4$/oxide nanocomposites.

| Nanocomposite	NaBH$_4$/Al$_2$O$_3$	NaBH$_4$/SiO$_2$
Enthalpy (J g^{-1}$_{nanocomposite}$)	1.92	9.82
Extraporous NaBH$_4$ (g g^{-1}$_{nanocomposite}$)	0.08	0.42
Fraction extra/intraporous NaBH$_4$	0.21:0.79	0.65:0.35
Percentage of scaffold pore volume filled	103%	46%

nanocomposite. This issue has not been encountered for $LiBH_4$/ oxide nanocomposites, because $LiBH_4$ has a lower surface tension γ_{lv} (0.12 N m^{-1}) compared to $NaBH_4$ (0.24–1.09 N m^{-1}) and therefore easily infiltrates the pores of both SiO_2 and Al_2O_3.[67]

Due to the decomposition of $NaNH_2$ upon melting (in the absence of ammonia back pressure) and the absence of low temperature structural phase transitions, it was not possible to study the incorporation of $NaNH_2$ in mesoporous metal oxides with DSC measurements, as this would require an ammonia overpressure during the measurements. Therefore, further evidence for the infiltration of $NaNH_2$ into the oxide pores is provided by XRD analysis and N_2 physisorption. The XRD diffraction patterns of the $NaNH_2/SiO_2$ and $NaNH_2/Al_2O_3$ nanocomposites are shown in Figure 2b. For comparison, the XRD patterns of pure $NaNH_2$ and a physical mixture of $NaNH_2$ and the metal oxide are included. Interestingly, the sharp crystalline peaks that are observed in the diffraction patterns of the pure compound and the physical mixtures (PM), are not present for the nanocomposites. The XRD diffraction peaks for $NaNH_2$ are less intense in both $NaNH_2/SiO_2$ and $NaNH_2/Al_2O_3$. This absence of long-range crystallinity is attributed to successful incorporation of $NaNH_2$ in the oxide pores, since confined $NaNH_2$ forms nanosized crystallites in the oxide pores which cannot be probed by XRD.[67,70] Moreover, the successful incorporation of $NaNH_2$ into the mesoporous oxides is further confirmed by results from N_2 physisorption. The physisorption curves and corresponding pore size distributions of $NaNH_2/Al_2O_3$ and $NaNH_2/SiO_2$ nanocomposites with different pore filling fractions are shown in **Figure 3** and Figure S3 (Supporting Information), respectively. Here, a loss in pore volume is observed with increasing amount of $NaNH_2$, consistent with gradual infiltration of the metal hydride in the scaffold pores.[38,70] At low pore filling fractions (15%), a partial loss of the pore volume is observed, which indicates that the loss in pore volume is not caused by pore blockage. Hence, it is clear that $NaNH_2$ is readily incorporated in both mesoporous oxide scaffolds, in line with the DRIFTS and XRD results.
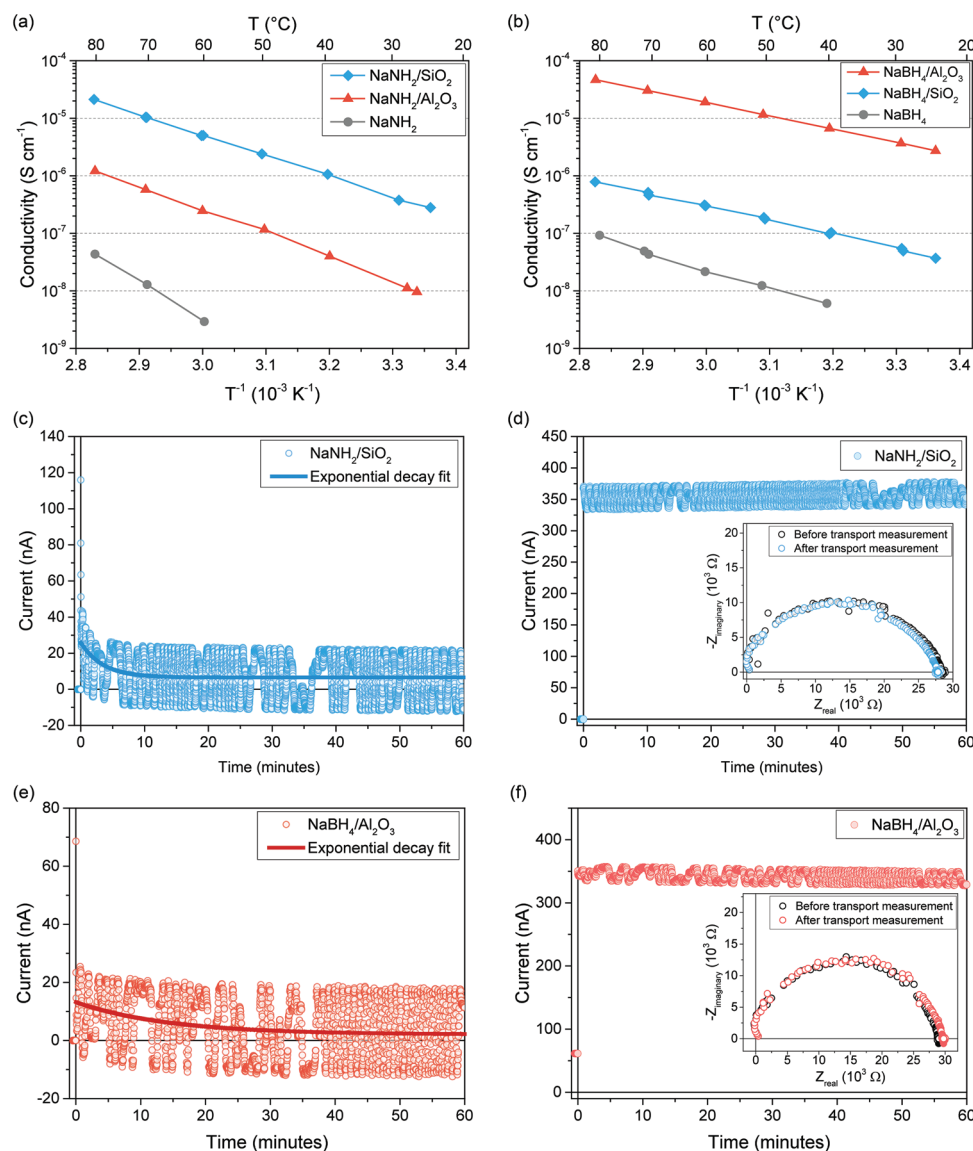
2.2. Na-Ion Conductivity in $NaBH_4$- and $NaNH_2$/Oxide Nanocomposites

To investigate the effect of the nanocomposite formation on the Na-ion conductivity, the impedance of the $NaBH_4$- and $NaNH_2$/ oxide nanocomposites was determined by EIS. The nanocomposites discussed here contain a $NaBH_4$ or $NaNH_2$ volume that is equal to 130% of the total pore volume of the oxide scaffolds. In this way, the metal hydride can in theory completely fill the pores of the scaffold, while also covering the outer surface of the scaffold, ensuring a percolating network of fast Na$^+$ diffusion pathways over the non-conducting oxide particles. The temperature-dependent Na-conductivities as derived from the complex impedance analysis are displayed in **Figure 4**a for $NaNH_2$/oxide nanocomposites and Figure 4b for $NaBH_4$/ oxide nanocomposites, as well as the corresponding electronic and Na-ion transport measurements (Figure 4c–f). The corresponding single arc Nyquist plots and fitted values are reported in Figure S4 (Supporting Information). The reversible behavior during heating and cooling is shown in Figure S5a (Supporting Information) and indicates that the changes to the material during cycling are negligibly small. In Figure S5b (Supporting Information), the conductivity data of physically mixed $NaNH_2$-Al_2O_3 and $NaBH_4$-SiO_2 samples with same concentration as the 130% pore filled nanocomposites, are shown. The very low conductivity of these physically mixed samples demonstrates that the formation of a nanocomposite is required to achieve improved conductivity. Details on the electrochemical stability and galvanostatic cycling of the nanocomposites can be found in Figures S6 and S7 (Supporting Information).

The data depicted in Figure 4 demonstrate that over the entire temperature range from room temperature to 80 °C all nanocomposites display an enhancement of the conductivity compared to pristine sodium compounds. The electronic and Na-ion transport measurements (Figure 4c–f) confirm that for both the $NaNH_2$- and $NaBH_4$/oxide nanocomposites, the conductivity determined from EIS corresponds directly to Na-ion transport, as the electronic transport is negligible and the Na-ion transport number is almost unity. Notably, for the
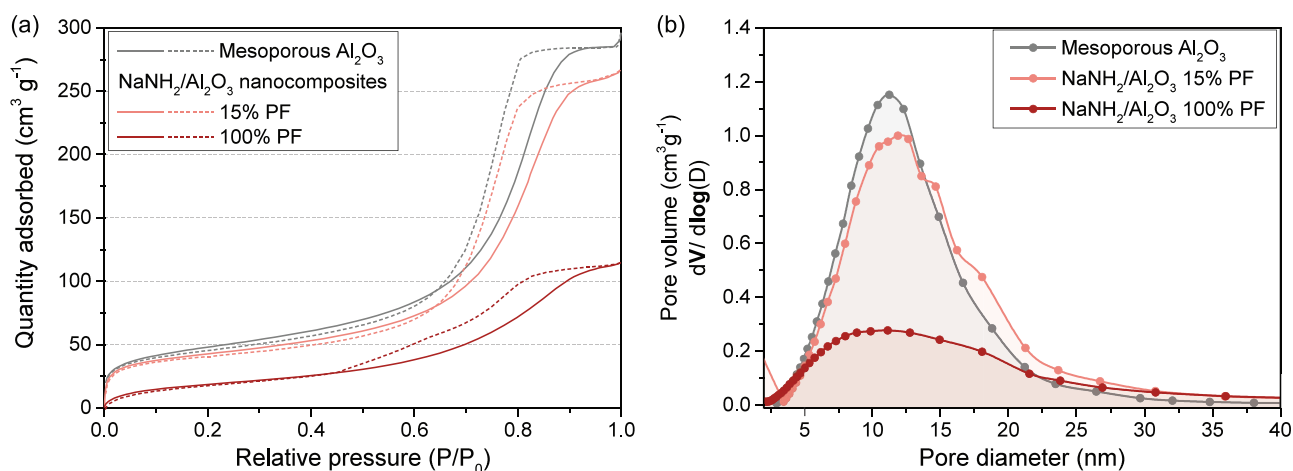
Figure 3. a) N_2 physisorption isotherms and b) corresponding pore size distribution of $NaNH_2/Al_2O_3$ nanocomposites with pore filling fractions of 15% and 100%. The isotherm of pristine Al_2O_3 is provided for comparison. The solid lines correspond to adsorption curves and the dashed lines correspond to desorption curves. The pore size distribution is determined from the BIH adsorption curve using the standard Harkins and Jura analysis.

**ADVANCED
SCIENCE NEWS**

www.advancedsciencenews.com

**ADVANCED
FUNCTIONAL
MATERIALS**

www.afm-journal.de

Figure 4. Arrhenius plots of Na-ion conductivity versus reciprocal temperature of a) NaBH$_4$/oxide and b) NaNH$_2$/oxide nanocomposites based on SiO$_2$ (blue) and γ-Al$_2$O$_3$ (red) with 130% pore filling fraction, as well as pure NaBH$_4$ or NaNH$_2$. The first temperature-dependent heating cycle is shown. c–f) Electronic and Na-ion transport measurements on NaNH$_2$/SiO$_2$ c,d) and NaBH/Al$_2$O$_3$ symmetric cells. The electronic measurements (c,e) were performed on symmetric cells with blocking electrodes (SS) and Na-ion measurements (d,f) have been performed on symmetric cells with non-blocking electrodes.

NaNH$_2$/oxide nanocomposites (Figure 4a), the NaNH$_2$/SiO$_2$ sample possesses the highest conductivity (2.12 × 10^{-5} S cm^{-1} at 80 °C), about three orders of magnitude higher than pristine NaNH$_2$ (4.35 × 10^{-8} S cm^{-1} at 80 °C). The Na-ion conductivity of the NaNH$_2$/Al$_2$O$_3$ nanocomposite is 1.22 × 10^{-6} S cm^{-1} at 80 °C, higher than that of pristine NaNH$_2$, but below that of NaNH$_2$/SiO$_2$. Contrarily, the NaBH$_4$/oxide nanocomposite based on Al$_2$O$_3$ exhibits the highest Na-ion conductivity (4.66 × 10^{-5} S cm^{-1} at 80 °C) for the NaBH$_4$ nanocomposites (Figure 4b), while the Na-ion conductivity of the NaBH$_4$/SiO$_2$ is significantly lower, i.e., 7.85 × 10^{-7} S cm^{-1}. Both nanocomposites show an improvement compared to pure NaBH$_4$ (9.23 × 10^{-8} S cm^{-1} at 80 °C) of, respectively, almost three orders of magnitude and a 70-fold increase. To compare, for LiBH$_4$

an increase over three orders of magnitude upon confinement in a similar SiO$_2$ scaffold (MCM-41) is typically observed.[71] Hence, while it is evident that nanocomposite formation leads to conductivity improvement for sodium-based complex hydrides analogous to lithium borohydride, the exact extent of the enhancement clearly differs from the lithium-based counterparts.

The temperature-dependence of the ion conductivity (σ) indicates Arrhenius type behavior in the applied temperature range. This Arrhenius behavior is described by $\sigma(T) = \frac{\sigma_0}{T} e^{-E_A/k_B T}$, where k_B is the Boltzmann constant, σ_0 is a pre-exponential factor, and E_A is the activation energy.[72] Accordingly, the activation energy for long-range ion transport in the nanocomposites

Table 2. Activation energy (E_A) and ln (σT) obtained from a linear plot of ln (σT) and 10^{-3} T^{-1} of the second temperature dependent EIS cycle reported in Figure 3. The standard deviation is based on the 95% confidence interval of the linear fit.

Metal hydride/(oxide)	ln σ_0	E_A [eV]
Pristine NaNH$_2$	34 ± 17	1.4 ± 0.5
NaNH$_2$/SiO$_2$	19.1 ± 0.6	0.73 ± 0.02
NaNH$_2$/Al$_2$O$_3$	20 ± 1	0.85 ± 0.04
Pristine NaBH$_4$	12 ± 3	0.67 ± 0.07
NaBH$_4$/SiO$_2$	8.6 ± 0.5	0.51 ± 0.01
NaBH$_4$/Al$_2$O$_3$	11.7 ± 0.1	0.48 ± 0.01

could be derived by linearly fitting the data shown in Figure 4. A summary of the calculated activation energies is reported in **Table 2**. The activation energy of the NaNH$_2$/oxide nanocomposites (0.73 and 0.85 eV for NaNH$_2$/SiO$_2$ and NaNH$_2$/Al$_2$O$_3$, respectively) is considerably lower than the value obtained for pristine NaNH$_2$ (1.4 eV). The lowest activation energy is obtained for the most conductive NaNH$_2$/oxide nanocomposite, NaNH$_2$/SiO$_2$. Likewise, the activation energies of the NaBH$_4$/oxide nanocomposites display the same trend, i.e., a decreasing of the E_A after nanocomposite formation. The calculated activation energies for NaBH$_4$/SiO$_2$ and NaBH$_4$/Al$_2$O$_3$ are 0.51 and 0.48 eV, smaller than the activation energy of 0.67 eV calculated for pristine NaBH$_4$. Hence, in agreement with the enhancement in conductivity, the activation energy for ion transport has decreased upon nanocomposite formation, in agreement with the behavior that has previously been established for LiBH$_4$ nanocomposites.[36,41,44,71] When comparing the conductivities and activation energies of the NaNH$_2$/oxide nanocomposites and the NaBH4/oxide nanocomposites, it is observed that the largest conductivity improvement is achieved with a different scaffold, SiO$_2$ in the case of NaNH$_2$ and Al$_2$O$_3$ in the case of NaBH$_4$. The origin of this behavior will be discussed in detail later.

Before discussing the differences between the NaNH$_2$- and NaBH$_4$-nanocomposites, the effect of the metal hydride-to-metal oxide weight ratio (or pore filling) in the nanocomposite on the Na-ion conductivity will be considered. Here, we specifically analyzed the composition dependence for the NaBH$_4$/Al$_2$O$_3$ nanocomposite, as this system demonstrated the highest Na-ion conductivity. The explored composition ranges from a NaBH$_4$:Al$_2$O$_3$ weight ratio of 0.26:1 to a ratio of 0.88:1, which corresponds to a pore filling fraction of 50–170% (see Table S2, Supporting Information). The Arrhenius plots for the conductivities of these NaBH$_4$/Al$_2$O$_3$ samples are displayed in **Figure 5**a. The dependence of the activation energy and Na-ion conductivity (at 50 °C) on the pore filling is shown in Figure 5b. The highest σ value at 50 °C is reached for a pore filling fraction of 120–130% confirming the trend that has been previously reported. The Na-ion conductivity increases with the increasing amount of NaBH$_4$ up to a pore filling fraction of 130%, while the conductivity decreases after exceeding this value. This can be explained by the presence of non-conducting phases in the NaBH$_4$/Al$_2$O$_3$ composites. A pore filling fraction that is lower than 120% would result in an excess of insulating Al$_2$O$_3$ that interrupts the Na-ion diffusion pathways, thereby decreasing Na-ion conductivity. On the other hand, if the volume pore filling (volume of NaBH$_4$ in the Al$_2$O$_3$ pores) exceeds 130%, long-range Li-ion transport is hindered by the presence of the poorly conducting macrocrystalline NaBH$_4$. It is worth noting that the calculated E_A values confirm this behavior as well. In fact, the E_A decreases up to 0.46 eV for a pore filling fraction of 130%, verifying that this is the optimal composition for the metal hydride nanocomposites. When the amount of NaBH$_4$ is increased or decreased, the activation energy increased, indicating less favorable Na-ion conduction pathways.

These results are in line with the ones reported by Gulino et al., which revealed a maximum of the Li-ion conductivity for the system LiBH$_4$-SiO$_2$ system for a complete pore volume filling (i.e., 100%).[41] The slight difference in the composition for the maximum σ value can be explained considering the two different routes used to synthetize the nanocomposites, i.e., ball milling for Gulino et al. and melt infiltration in this work that typically requires a larger pore filling.[42,73] For the first time, we have described how the structural parameter pore filling affects the Na-ion conductivity in sodium composite electrolytes synthetized via melt infiltration. It is important to consider that
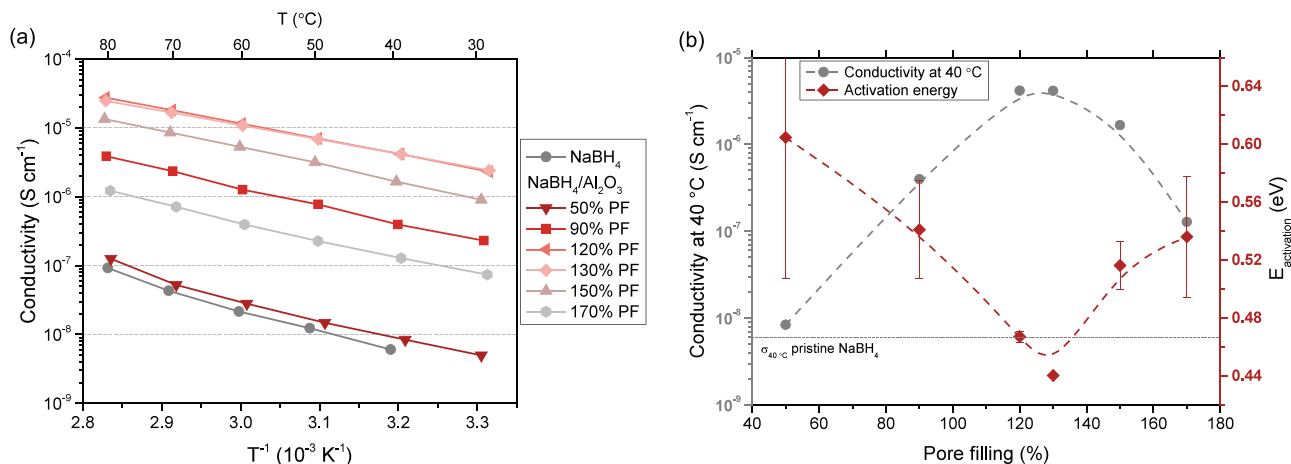
Figure 5. a) Arrhenius plots of Na-ion conductivity versus reciprocal temperature of NaBH$_4$/Al$_2$O$_3$ nanocomposites with varying pore filling. b) Na-ion conductivity at 50 °C (grey circles) and activation energy (red squares) as a function of pore filling (%) dashed lines are added as guide to the eye.

**ADVANCED
SCIENCE NEWS**

www.advancedsciencenews.com

**ADVANCED
FUNCTIONAL
MATERIALS**

www.afm-journal.de

this optimum in pore filling will not apply to nanocomposites in which the metal hydride does not completely infiltrate the scaffold pores, such as the $NaBH_4/SiO_2$ nanocomposite, as in this case more extraporous (macrocrystalline) metal hydride that can hinder long-range ionic transport is present in the nanocomposite.

## 2.3. Probing the Conductive Metal Hydride-Oxide Interface

The improved Na-ion conductivity observed for the $NaNH_2$/oxide and $NaBH_4$/oxide nanocomposites could originate from the creation of a highly conductive interface layer at the metal hydride-metal oxide interface during the synthesis of the nanocomposites, as reported for $LiBH_4$/oxide nanocomposites. For $LiBH_4$, it has been demonstrated that the enhancement in conductivity upon nanocomposite formation with a mesoporous oxide originates from interactions between surface groups of the oxide and the metal hydride.[36,37,43,74] This interface layer is characterized by high ion dynamics for both BH_4^- and Li^+ but has not yet been defined with a clear crystal structure.[40,73] Similarly, de Kort et al. recently identified comparable interface-induced ionic conductivity in $LiBH_4$-$LiNH_2$/oxide nanocomposites.[42] The physical and chemical properties of the oxide materials were shown to be critical for the interface reaction, and thereby the ionic conductivity of the nanocomposite materials, although the exact roles of the scaffold and the nature of the interface are not yet fully understood. Note that the interface layer is often referred to as a highly defected space charge layer, but considering the presence of strong interface interactions, and in some cases reactions, the formation of a tertiary phase at the interface should also be considered.

In the previous section, it was demonstrated that for both $NaBH_4$- and $NaNH_2$/oxide nanocomposites, the surface groups of the oxide scaffolds disappeared after melt infiltration due to interaction with the sodium metal hydrides (Figure 1). This suggests that also in the present case, interface reactions could have resulted in the formation of a conductive tertiary phase at the interface. Moreover, a remarkable difference in the ionic conductivity of $NaNH_2/SiO_2$ compared to $NaNH_2$/Al_2O_3, and $NaBH_4/SiO_2$ compared to $NaBH_4/Al_2O_3$, has been

observed (Figure 4). The highest conductivity for $NaNH_2$/oxide nanocomposites is obtained with the SiO_2 scaffold, while the $NaBH_4/Al_2O_3$ nanocomposite is more conductive than $NaBH_4/$ SiO_2. Evidently, the interaction of the two sodium compounds with SiO_2 and Al_2O_3 is distinctly different. This strongly suggests that the interface interaction does not only depend on the properties of the oxide scaffold, but also on the nature of the metal hydride.

In order to understand how the nanocomposite conductivity depends on the interactions between the metal hydride and the oxide scaffold, we have investigated the nature of the interface layer in the $NaBH_4/Al_2O_3$, $NaNH_2/Al_2O_3$, and $NaNH_2/SiO_2$ nanocomposites. The interface interactions in the $NaBH_4/SiO_2$ nanocomposite are not studied, since the metal hydride does not completely infiltrate the mesoporous oxide due to poor wetting of $NaBH_4$ on the SiO_2 surface as illustrated by DSC (Table 1). While it is likely that the $NaBH_4$ interacts with the SiO_2 surface in this case as well (though rather weakly), the overall conductivity is governed by the larger amount of macrocrystalline $NaBH_4$ outside of the scaffold pores. Consequently, it is not possible to fairly compare the results of this sample to the other nanocomposites.

To start, the metal hydride/oxide interface of the most conductive nanocomposite, $NaBH_4/Al_2O_3$, has been studied with DRIFTS and solid-state NMR (ssNMR). To this end, nanocomposites with low pore filling fractions were prepared to specifically probe the contribution of the $NaBH_4$-Al_2O_3 interface species, as the contribution of bulk-like $NaBH_4$ far away from the interface is minimized at these low metal hydride compositions. In **Figure 6**a, the DRIFTS spectra of $NaBH_4/$ Al_2O_3 with different pore filling fractions are shown. It can be observed that with decreasing pore filling, the vibrations at 3438 and 3275 cm^{-1} and between 2500 and 2000 cm^{-1} corresponding to $NaBH_4$ become increasingly less intense. At the same time, new peaks that are not associated with the γ-Al_2O_3 scaffold appear at 2547, 2473, 1760, and ≈1350 cm^{-1}, indicated by the dotted lines in Figure 6a. The peaks ≈2500 cm^{-1} are ascribed to B-H stretching vibrations in $Na_2B_{12}H_{12}$.[75–77] This indicates that near the scaffold surface $NaBH_4$ partially decomposes to form $Na_2B_{12}H_{12}$, as has already been demonstrated by Ngene et al. for $NaBH_4$/C nanocomposites.[78] Additionally, the
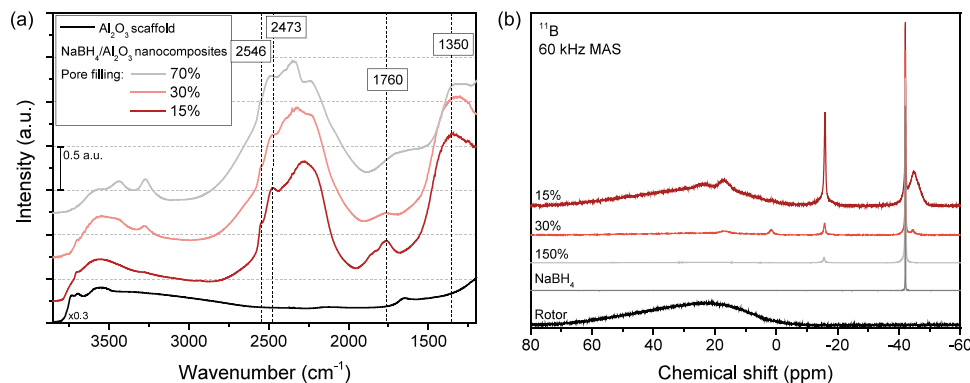
Figure 6. a) DRIFTS spectra of $NaBH_4/Al_2O_3$ nanocomposites with pore filling ranging from 15% to 70%. b) ^{11}B ssNMR spectra of pure $NaBH_4$, $NaBH_4/$ Al_2O_3 nanocomposites with 15%, 30%, and 150% pore filling and an empty NMR rotor. The nanocomposites spectra are normalized to the peak at −42 ppm. The spectrum of the empty rotor is normalized to the same value as the 15% pore filling composite for comparison of the background signal to the rotor.

vibrations at 1760 and 1350 cm^{-1} can be related to asymmetric stretching vibrations of B—O bonds in trigonal BO$_3$-units.[79,80] Hence, these results strongly suggest that the surface hydroxyl groups on Al$_2$O$_3$ react with NaBH$_4$ to form B—O bonds as well as Na$_2$B$_{12}$H$_{12}$, thereby forming a tertiary interfacial layer with enhanced Na-ion mobility.

High-resolution ssNMR measurements were performed on the NaBH$_4$/Al$_2$O$_3$ composites to further study the interfacial species present in the nanocomposites. In Figure 6b, the ^{11}B spectra for pristine NaBH$_4$, NaBH$_4$/Al$_2$O$_3$ nanocomposites with different pore filling and an empty sample holder (rotor) are shown. In Figure S8 (Supporting Information), an enlargement of the graph is provided in which the smaller peaks can be distinguished more easily. In the spectrum for pristine NaBH$_4$, a single peak is observed at a chemical shift of −42.0 ppm, ascribed to bulk-like [BH$_4^-$] species.[81] Compared to the pure NaBH$_4$ spectrum, the nanocomposite spectra contain several additional peaks. First of all, at a slightly more negative chemical shift of −44.8 ppm a broad peak is seen, which becomes more pronounced with lower pore filling fractions. This peak can be assigned to the presence of more shielded NaBH$_4$ nanoclusters, as has been previously reported for nanoconfined LiBH$_4$.[81] Secondly, in all nanocomposites, a peak is present at a chemical shift of −15.6 ppm, which corresponds to the presence of Na$_2$B$_{12}$H$_{12}$ in the samples.[81–83] Finally, in most of the NaBH$_4$/Al$_2$O$_3$ nanocomposite spectra, two peaks are seen at positive chemical shifts of 1.3 and 17.4 ppm, while the spectrum of the nanocomposite with a pore filling fraction of 15% contains a third peak at 24.4 ppm. Each of these peaks corresponds to a specific B—O species, respectively, tetragonal BO$_{4/2}^-$, trigonal BO$_{3/2}$, and three-coordinated BO$_{2/2}$O$^-$ sites.[84] This interaction of the [BH$_4^-$] anions with the oxide surface was investigated further with ^{27}Al ssNMR measurements. The ^{27}Al spectra of NaBH$_4$/Al$_2$O$_3$ with a low pore filling fraction (15%) and pristine γ-Al$_2$O$_3$ are displayed in Figure S9 (Supporting Information). The spectra demonstrate that the unsaturated penta-coordinated Al sites on the oxide surface become saturated upon incorporation of NaBH$_4$ in the scaffold pores, which can be attributed to coordination of the [BH$_4^-$] anion to the [AlO$_5$] on the oxide surface.[85–87] Thus, in line with the DRIFTS results, the ssNMR analysis confirms that incorporation of NaBH$_4$ in the Al$_2$O$_3$ scaffold results in the formation of

NaBH$_4$ nanoclusters, Na$_2$B$_{12}$H$_{12}$ and B—O species due to interaction with the oxide surface. The presence of B—O species has previously been associated with the formation of a conductive metal hydride/oxide interfacial layer in LiBH$_4$, LiBH$_4$-LiI, and LiF/Al$_2$O$_3$ nanocomposites.[33,44,86,88]

In a similar way, the interface interactions at the metal hydride-metal oxide interface in NaNH$_2$/Al$_2$O$_3$ and NaNH$_2$/SiO$_2$ nanocomposites have been studied with ssNMR and DRIFTS. Since boron is not present in these samples and ^{14}N and ^{15}N NMR did not give sufficient signal, the interfacial species were studied using ^{23}Na NMR and, for NaNH$_2$/Al$_2$O$_3$, ^{27}Al NMR. In **Figure 7**a, the ^{27}Al NMR spectra of NaNH$_2$/Al$_2$O$_3$ nanocomposites with pore filling fractions of 100% and 15% are shown, as well as pristine γ-Al$_2$O$_3$ for comparison. The pure γ-Al$_2$O$_3$ spectrum contains intense signals at 15 and 74 ppm, which reflect the presence of, respectively, six and fourfold-coordinated Al species.[85–87] A less intense signal is seen at 39 ppm, which represents unsaturated penta-coordinated Al ions near the surface of the oxide.[85–87] It is known that these penta-coordinated sites can serve as anchoring points for foreign anions such as F$^-$ from LiF or BH$_4^-$ from LiBH$_4$.[33,86] As a consequence, the penta-coordinated sites become saturated and the signal ≈39 ppm disappears. This phenomenon clearly occurs for the studied NaNH$_2$/Al$_2$O$_3$ nanocomposites as well. In the ssNMR spectra of both nanocomposites pronounced signals related to four and sixfold-coordinated Al species are present, while no signal related to penta-coordinated Al is observed. Hence, it seems likely that the NH$_2^-$ anion interacts with the [AlO$_5$] surface group, possibly forming a [AlO$_5$(NH$_2$)]-like species. In other conductor/insulator nanocomposites, such as LiF/Al$_2$O$_3$, the [AlO$_5$X] sites formed in this way significantly influence the overall ionic transport as Li$^+$ vacancies are created that can be utilized by other Li$^+$ ions to perform hopping processes in the interface region. Similarly, it is expected that the conduction in the NaNH$_2$/oxide nanocomposites depends on a surface-controlled diffusion mechanism.

The NMR signal related to fourfold-coordinated species consists of two peaks (at 84 and 75 ppm), which are clearly distinguishable in the NaNH$_2$/Al$_2$O$_3$ nanocomposite with a pore filling fraction of 15%. This indicates that in addition to the fourfold-coordinated Al species in pristine γ-Al$_2$O$_3$, a second fourfold-coordinated species is formed in the
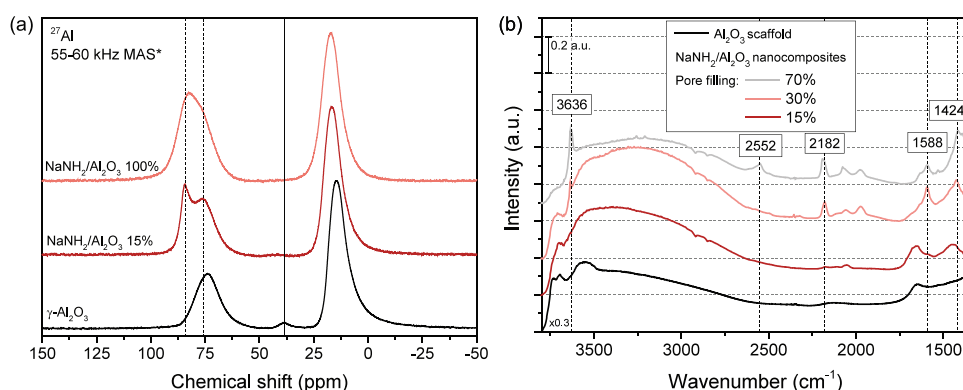
Figure 7. a) ^{27}Al ssNMR spectra of pure Al$_2$O$_3$ and NaNH$_2$/Al$_2$O$_3$ nanocomposites with 15% and 100% pore filling fraction. The nanocomposite spectra are normalized to the peak at 15 ppm. b) DRIFTS spectra of NaNH$_2$/Al$_2$O$_3$ nanocomposites with pore filling ranging from 15% to 70%.

nanocomposites due to interaction or reaction of the metal hydride with the Al_2O_3 surface. It is interesting to note that similar peaks are also present in the ^{27}Al NMR spectra of the $NaBH_4/Al_2O_3$ nanocomposites (Figure S9, Supporting Information). While the higher δ_{iso} of this $[AlO_4]$ species demonstrates that this compound has a higher Al—O bond order and shorter bonds,[87] ^{27}Al NMR does not provide further information on the possible nature of the interfacial compound(s) that might have formed. Therefore, the chemical nature of the $NaNH_2/Al_2O_3$ interface was investigated further with ^{23}Na NMR and DRIFTS analysis shown in Figure 7b and Figure S10 (Supporting Information). The ^{23}Na NMR spectra of heat-treated $NaNH_2$ and $NaNH_2/Al_2O_3$ with a pore filling fraction of 100% both exhibit a big quadrupolar feature with several peaks between 30 and −20 ppm. In contrast, the spectrum of the $NaNH_2/Al_2O_3$ nanocomposite with a pore filling fraction of 15% only displays two signals at 14 and −10 ppm. Evidently, two different Na species seem to have formed on the surface of the Al_2O_3 scaffold. From these measurements, it is not immediately clear to which Na-species these signals correlate. Possible compounds include Na_2O (−10 ppm),[89] NaN_3 (−11 ppm),[89] NaH (18 ppm),[90] $NaNO_3$ (−8.5 ppm),[91] and Na^+ ions coordinated to octahedral Al^{3+} (−8 and −14 ppm).[92,93] However, further investigation is required to confirm the assignment of both peaks.

In the DRIFTS spectra of the $NaNH_2/Al_2O_3$ nanocomposites, five peaks are observed, at 3636, 2552, 2182, 1588, and 1424 cm^{-1}, that are not observed for pristine $NaNH_2$, heat-treated $NaNH_2$, or the $NaNH_2/Al_2O_3$ nanocomposites with a pore filling fraction of 130% (Figure 1b). Interestingly, the DRIFTS spectrum of pristine Na_2O (Figure S11, Supporting Information) displays a sharp peak at exactly 3636 cm^{-1} as well, coupled with a broad peak ≈1450 cm^{-1}. In line with the ^{23}Na NMR results, this indicates that Na_2O might have formed at the $NaNH_2/Al_2O_3$ interface. While the assignment of the peaks at 2552, 2182, and 1588 cm^{-1} to specific compounds is less evident, in most cases they point toward the formation of N—O species. For example, the peak at 2180 cm^{-1} is often assigned to N—O vibrations in NO^+. Likewise, the peak at 1588 cm^{-1} could

be ascribed to N—O vibrations related to NO_2^- and NO_3^-.[94–96] Thus, both ssNMR and DRIFTS analysis demonstrate that $NaNH_2$ interacts with the surface groups of Al_2O_3, akin to $NaBH_4/Al_2O_3$, thereby possibly forming Na_2O and N—O-containing interfacial compounds.

Note that the $NaNH_2/Al_2O_3$ nanocomposite is less conductive than the nanocomposite based on SiO_2. Consequently, it is interesting to see whether in $NaNH_2/SiO_2$ different and possibly more conductive interfacial compounds have formed. In **Figure 8**, the DRIFTS spectra and ^{23}Na NMR spectra of $NaNH_2/SiO_2$ nanocomposites with a pore filling fraction of 100%, 30%, and 15% are shown. First of all, in the DRIFTS spectra of the $NaNH_2/SiO_2$ nanocomposites, five new peaks are observed at 3636, 3506, 3438, 2182, and 1424 cm^{-1}. Interestingly, none of them correspond to pristine $NaNH_2$, heat-treated $NaNH_2$, or the $NaNH_2/SiO_2$ nanocomposite with a pore filling fraction of 130% (Figure 1b). Three of these peaks (3636, 2182, and 1418 cm^{-1}) were also observed in the $NaNH_2/Al_2O_3$ nanocomposites with low pore filling fraction (Figure 7b) and can correspondingly be assigned to the presence of Na_2O and possibly NO-containing compounds. In contrast, the two remaining peaks at 3506 and 3438 cm^{-1} are only seen in the $NaNH_2/SiO_2$ nanocomposites. Generally, peaks in the region between 3600 and 3300 cm^{-1} can be assigned to O—H[95–98] and N—H vibrations.[61,62,96,99] Here, these peaks might have appeared, because the vibrational energy of the surface hydroxyl groups or the N—H groups in $[NH_2]^-$ has changed due to interaction between the oxide surface and the metal hydride. Different from the $NaNH_2/Al_2O_3$ nanocomposite, it seems that the $[NH_2]^-$ anions interact weakly with the SiO_2 surface and consequently the anions stay intact and it is less likely that NO-containing compounds form at the interface. This is in line with the different activation energies found for ion conduction in the $NaNH_2$/oxide nanocomposites (Table 2), which indicates that the ion conduction mechanism differs between the nanocomposites, suggesting the formation of different interfacial compounds.

These results are further corroborated by the ^{23}Na NMR measurements shown in Figure 8b. Similar to the results on
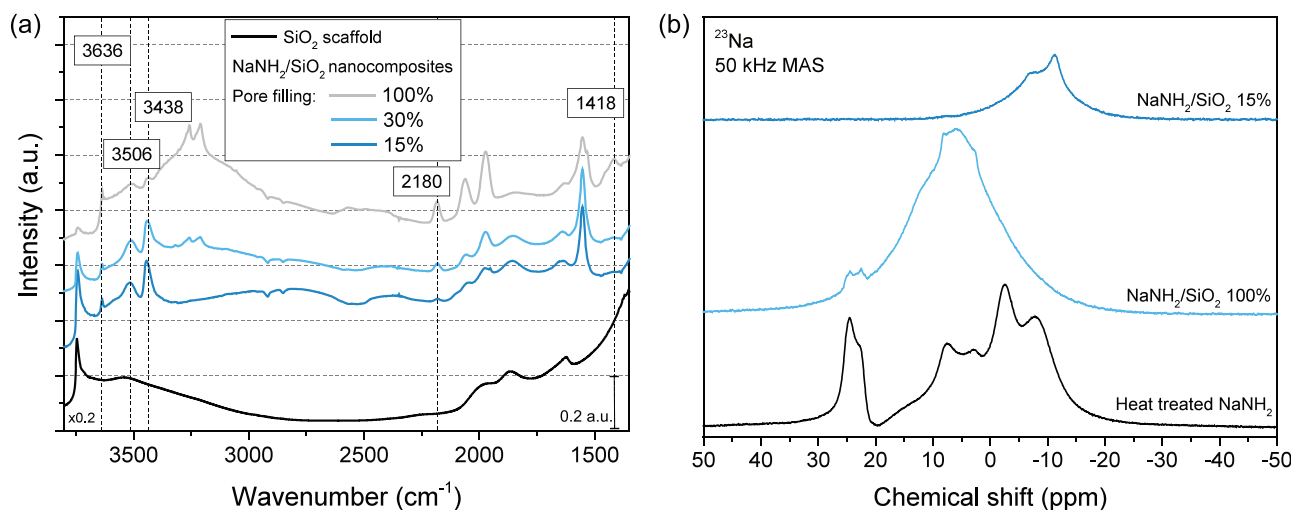
Figure 8. a) DRIFTS spectra of $NaNH_2/SiO_2$ nanocomposites with pore filling ranging from 15% to 100%. b) ^{23}Na ssNMR spectra of heat $NaNH_2$ and $NaNH_2/SiO_2$ nanocomposites with 15% and 100% pore filling.

ADVANCED
SCIENCE NEWS

www.advancedsciencenews.com

ADVANCED
FUNCTIONAL
MATERIALS

www.afm-journal.de

$NaNH_2/Al_2O_3$, the ^{23}Na NMR spectra of $NaNH_2/SiO_2$ with a pore filling fraction of 100% and 15% are distinctly different. While the former exhibits a broad quadrupolar feature with several peaks between 30 and –10 ppm, the latter contains only two signals at –7.5 and –11 ppm. The signal at –11 ppm could be related to the presence of Na_2O, akin to the signal at –10 ppm found for $NaNH_2/Al_2O_3$. The signal at –7.5 ppm has not been observed for $NaNH_2/Al_2O_3$ and could therefore be attributed to the unidentified interface compound revealed with DRIFTS. The chemical shift of this signal is comparable to that of published values for Na^+ ions in silica matrixes, such as $Na_2Si_2O_5$ and $NaAlSi_3O_8$.[100–102] It is important to realize that the interface compounds are typically defected and non-stoichiometric, which means that the local ^{23}Na environment will differ, resulting in a different chemical shift. As a result, it is not possible to determine the exact structure of the hydride/oxide interface. Nevertheless, this analysis clearly shows that in the $NaNH_2/SiO_2$ and $NaNH_2/Al_2O_3$ nanocomposites different interfacial compounds have formed. Additionally, similarities and differences with the $NaBH_4$-based counterparts are identified. In the next section, the similarities and differences between both metal hydrides will be compared and the implications they have on the ionic conductivities of the corresponding nanocomposites will be discussed.

3. Conclusion

With the DRIFTS and ssNMR results discussed in the previous section, it was possible to verify that a tertiary phase is formed at the metal hydride-metal oxide interface in the studied nanocomposites, i.e., $NaBH_4/Al_2O_3$, $NaNH_2/Al_2O_3$, and $NaNH_2/SiO_2$. In both Al_2O_3-containing nanocomposites, penta-coordinated Al-surface species become saturated upon incorporation of the metal hydride via melt infiltration. When $NaBH_4$ is incorporated, $Na_2B_{12}H_{12}$ and B−O bonds are formed at the metal hydride-oxide interface. Likewise, upon infiltration of $NaNH_2$ in the Al_2O_3 pores, an interfacial layer containing Na_2O and N−O species seems to form. The saturation of Al-surface species combined with the formation of B−O and N−O bonds demonstrates that there is a strong interaction between both metal hydrides and the Al_2O_3 surface. In contrast, it seems that in the $NaNH_2/SiO_2$ nanocomposites the interaction between the silica surface and the metal hydride is weak, since in this case the $[NH_2]^-$ anions at the interface remain (partially) intact.

The differences in the interface composition can be ascribed to the different surface chemistry of the oxide scaffolds. Both the amount and nature of surface hydroxyl groups differ greatly between SiO_2 and Al_2O_3. A high density of surface hydroxyl groups is observed for Al_2O_3, which contains ≈10 hydroxyl groups per nm^2, while SiO_2 only contains 4–5.5 groups per nm^2.[103] Moreover, in contrast to the weakly (Brønsted) acidic hydroxyl groups present on the SiO_2 surface, Al_2O_3 contains strong surface groups with both (Lewis) acidic and basic character (Figure S12, Supporting Information). With this in mind, it is evident that the Al_2O_3 scaffold interacts more strongly with the metal hydrides than SiO_2. However, this does not explain why a stronger interface interaction leads to higher conductivity for $NaBH_4/Al_2O_3$, but a lower conductivity for $NaNH_2/Al_2O_3$.

Previous studies on $LiBH_4$- and $LiBH_4$-$LiNH_2$/oxide nanocomposites have shown that a higher number of surface groups or stronger surface groups lead to a higher conductivity.[37,42,43] This also seems to be applicable for $NaBH_4$/oxide nanocomposites. For $NaBH_4$, a strong interaction with the oxide, and therefore improved wettability, is both beneficial for the complete incorporation in the pores of the scaffold as well as for the formation of a conductive interface consisting of $NaBH_4$, $Na_2B_{12}H_{12}$, and B−O bonds between the metal hydride and the oxide surface. This is in line with results on $LiBH_4$/oxide nanocomposites reported by Choi et al., where a more conductive interface layer is formed in $LiBH_4/\gamma$-Al_2O_3 compared to $LiBH_4/SiO_2$.[37] On the other hand for $NaNH_2$, a strong interaction seems to be disadvantageous for $NaNH_2$/oxide nanocomposites. In this case, a strong interaction is not needed to incorporate $NaNH_2$ in the scaffold pores, since it easily wets both the SiO_2 and Al_2O_3 surface, and is thereby readily incorporated in both scaffolds. Furthermore, the formation of N−O species Na_2O resulting from a strong interaction between $NaNH_2$ and the Al_2O_3 surface does not seem to result in a conductive interface layer. Instead, the weaker interaction with the silica surface in which the amide anion remains intact yields a higher nanocomposite conductivity, likely resulting in a more conductive metal hydride-oxide interface layer with a lower activation energy for long-range ionic transport.

Although the exact composition of the interface layers is still not yet clear, the low conductivity of the physically mixed $NaBH_4$-Al_2O_3 and $NaNH_2$-SiO_2 (Figure S5b, Supporting Information) for which interface reactions are not expected, is clear evidence that the increased conductivity in the nanocomposites is indeed related to this interface reactions. The DRIFTS and NMR results suggest highly defected/disordered structures, as would be expected from such interface reactions. We therefore attribute the increased conductivity to the high number of defects/vacancies in the nanocomposites, which are known to lead to orders of magnitude increase in ionic conductivity, and in some cases lower activation energy of ion migration in composite materials.[36,37,43,74]

The differences in conductivity of these complex hydride-based nanocomposites can be explained by their stability or reactivity. Based on their melting points and decomposition temperature, it is clear that $NaNH_2$ is a less stable and more reactive compound compared to $NaBH_4$ and $LiBH_4$.[104–106] It therefore interacts more strongly with the mesoporous oxide scaffolds. Consequently, $NaNH_2$/oxide nanocomposites do not benefit much from a strong interface reaction, while it is a requirement for $NaBH_4$/oxide nanocomposites. On the other hand, $LiBH_4$ has an intermediate stability compared to $NaNH_2$ and $NaBH_4$, so upon nanocomposite formation with Al_2O_3 and SiO_2 a conducting interface layer forms in both cases resulting in comparable conductivities.[44,74] These results highlight that, since the conductivity enhancement in metal hydride/oxide nanocomposites originates from the formation of a tertiary phase at the hydride-oxide interface, both the surface chemistry of the mesoporous oxide and the reactivity of the metal hydride should be considered. While the pore structure of the scaffold can affect the conductivity of nanocomposites, in the present case it is clear that the chemical nature of the oxides plays a more important role in determining the ionic conductivity.

To conclude, in this work the effect of nanocomposite formation with oxide scaffolds on the ionic conductivity of sodium-based complex hydrides ($NaNH_2$ and $NaBH_4$) has been investigated. The study reveals that the Na-ion conductivity can be increased by three orders of magnitude to ionic conductivities of 4.66×10^{-5} and 2.12×10^{-5} S cm^{-1} at 80 °C, respectively, for $NaBH_4/Al_2O_3$ and $NaNH_2/SiO_2$. DRIFTS and NMR measurements show that this is related to the formation of highly distorted interface structures. Therefore, without ruling out the possible effects of space charge layer, we have shown for the first time that the enhancement in the nanocomposites conductivity results from the formation of a tertiary phase at the metal hydride-oxide interface, which strongly depends on the properties of the metal hydride and the mesoporous oxide that are used. A detailed investigation of the interactions between the metal hydrides and oxide scaffolds has shown that both the surface chemistry of the oxide scaffolds and reactivity of the complex hydrides are critical for the ionic conductivity of sodium-based nanocomposite electrolytes. The findings in this work demonstrate that moderate interface interaction between the oxides and metal hydrides is required to form a highly conductive metal hydride/oxide nanocomposite. This insight is imperative for the rational design of novel nanocomposite-based solid ion conductors. Using this guideline, the design principle as proposed by Gulino et al. can be extended from $LiBH_4$-based nanocomposites to other metal hydride/oxide ion conductors.[74] All in all, this study demonstrates that nanocomposite formation is an easy and versatile approach to enhance the ionic conductivity of both Li- and Na-based complex hydrides.

4. Experimental Section

Scaffold Preparation: Mesoporous silica MCM-41 was synthesized following the procedure of Cheng et al.[52] Hexadecyltrimethylammonium bromide (CTAB, Sigma–Aldrich, ≥96.0%) and tetramethylammonium hydroxide solution (TMAOH, Sigma–Aldrich, 25 wt.% in H_2O) were mixed with 300 mL deionized water. As a silica source, Aerosil 380 (Evonik) was added to the mixture and the suspension was stirred for 2 h at 30 °C. The mixture was aged at 30 °C for 24 h without stirring in a closed polypropylene bottle. The composition of the mixture had a molar ratio of 1.00 SiO_2:0.19 TMAOH:0.27 CTAB:40 H_2O. The obtained gel mixture was transferred to a Teflon-line stainless steel autoclave and was left to react for 40 h in a 140 °C pre-heated oven. The product was filtered and washed with deionized water to remove surfactants. The wet product was dried in static air at 120 °C for 8 h. The dried product was calcined under static air for 12 h at 550 °C (1.5 °C min^{-1}). Alumina (γ-Al_2O_3, Puralox SCCa-5/200, Sasol) was purchased and used without any further modifications. Alumina and as-synthesized MCM-41 were dried under nitrogen flow at 300 °C for 6 h and subsequently stored in an Ar-filled glovebox (H_2O, $O_2 < 1$ ppm).

To probe the porosity of the mesoporous oxides and nanocomposites, nitrogen physisorption measurements were performed on a Micromeritics Tristar 3000. Using the Brunauer–Emmett–Teller (BET) and Barrett–Joyner–Halenda (BJH) adsorption model theories, surface area and pore size distribution were obtained.[53,54] The specific surface area (A_{BET}), total pore volume, and average pore size as determined from the adsorbed quantity close to nitrogen saturation pressure ($p = p_0$) are summarized in Table S1 (Supporting Information). Scanning electron microscopy (SEM) images were obtained on a Thermo Fisher FEI XL30 SFEG instrument operating at an acceleration voltage of 5 kV measuring secondary electrons on a Through-Lens-Detector.

Samples were sputter-coated with ≈8 nm of Pt before loading into the SEM instrument. The obtained SEM images are shown in Figure S1 (Supporting Information).

Nanocomposite Synthesis: Preparation of $NaBH_4$ and $NaNH_2$/oxide nanocomposites had been performed via melt infiltration. $NaBH_4$ (Sigma–Aldrich, 99.99 %, trace metals basis) and $NaNH_2$ (Sigma–Aldrich, 98 %) were stored and handled in an Ar-filled glovebox to avoid exposure to air (H_2O, $O_2 < 1$ ppm). The melt infiltration synthesis was started by hand mixing the Na-salt with the appropriate amount of oxide in an agate mortar for ≈15 min. The amount of $NaBH_4$ or $NaNH_2$ in mixture is based on the pore volume of the oxide scaffold and the chosen pore filling fraction in the nanocomposite, i.e., the percentage of the scaffold pores that is filled with $NaNH_2$ or $NaBH_4$. An overview of the composition of the investigated nanocomposites is provided in Table S2 (Supporting Information). In some cases, the pore filling percentage was >100%, i.e., larger than the total pore volume of the scaffold. This ensures a percolating network of fast Na$^+$ diffusion pathways on the outer surface of non-conducting oxide particles. After extensive mixing, the physical mixtures (PMs) were placed in a quartz ($NaNH_2$) or alumina ($NaBH_4$) reactor within a stainless-steel autoclave. Prior to the synthesis, the autoclave is pressurized with either 8 bar of NH_3 or 5 bar of H_2 to prevent decomposition of $NaNH_2$ and $NaBH_4$, respectively. Finally, melt infiltration was carried out for 30 min at either 225 °C (heating rate = 2.5 °C min^{-1}) for $NaNH_2$ and at 525 °C (heating rate = 3.5 °C min^{-1}) for $NaBH_4$. Upon cooling, the molten sodium salts solidify in the pores of the scaffold material to form nanoconfined $NaNH_2$ and $NaBH_4$. After cooling to room temperature, the air-tight autoclaves were removed from the furnace and brought inside the glovebox. For the $NaNH_2$/oxide nanocomposites, the NH_3 pressure was released before removing from the synthesis set-up, while the H_2 pressure used during the $NaBH_4$ melt infiltration was released in the glovebox. Subsequently, the nanocomposites were stored in an Ar-filled glovebox and all further sample handling, characterization and measurements were performed under inert atmosphere either in the glovebox or using airtight sample holders.

Electrochemical Characterization: The conductivity of the pristine metal hydrides and nanocomposites was measured with EIS using a Princeton Applied Research Parstat 2273 potentiostat placed in a custom made Büchi B-585 glass oven. Using a standard 13 mm pellet press, ≈150–250 mg was pressed between stainless-steel electrodes covered with sodium foil with a pressure of 150 MPa. Using this method, pellets with a thickness of 1.0–1.5 mm were obtained.

The EIS measurements have been performed by incrementally heating the samples from RT to 80 °C ($\Delta T = 10$ °C) and then incrementally cooling to RT ($\Delta T = 20$ °C). Since the melting temperature of Na metal is 98 °C, 80 °C was the maximum temperature that could be used. At each increment, the temperature was allowed to equilibrate for 45 min, after which an EIS measurement was acquired with a 20 mV rms modulated alternating current potential in a frequency range from 1 MHz to 1 Hz. The complex impedance spectra were fitted to a least squares minimum with a circuit consisting of a resistor (R) in parallel with a constant phase element (CPE). Based on the obtained resistance value, the electrode area (A = 1.33 cm^2) and thickness (t) of the pellet, the conductivity, σ, was calculated via $\sigma = t/AR$.

The electronic and Na-ion transport numbers have been determined using DC voltage polarization measurements.[34,55,56] The $NaBH_4/Al_2O_3$ and $NaNH_2/SiO_2$ nanocomposites were pressed into a pellet between two stainless steel cylinders (Ø = 10 mm) with a pressure of 190 MPa. In case of the Na-ion transport measurements sodium foil was placed on either side of the pellet after pelletization, after which the cell is closed hand-tight. The cell is allowed to equilibrate at 60 °C for at least 1 h. Subsequently, a voltage of 0.5 V (electronic transport) or 0.01 V (Na-ion transport) was applied across the pellet and the resulting current was measured for 1 h using a Parstat PMC-1000 potentiostat. The total conductivity was obtained by performing an EIS measurement using a 20 mV RMS modulated AC potential with frequencies from 1 MHz to 1 Hz before and after the polarization measurement. The ionic transport number (t_{ion}) is determined using the equation, $t_{ion} = (I_{total} - I_e)/I_{total}$,

**ADVANCED
SCIENCE NEWS**

www.advancedsciencenews.com

**ADVANCED
FUNCTIONAL
MATERIALS**

www.afm-journal.de

where I_e is the steady-state electronic current. The Na-ion transport number (t_{Na}) could be estimated based on the steady-state current I_{Na} and the initial current I_0, combined with the resistance before (R_0) and after (R_{after}) the transport measurement using the following formula:

$$t_{Na} = \frac{I_{Na}}{I_0} \cdot \frac{\Delta V - I_0 R_0}{\Delta V - I_{Na} R_{after}}.$$

Galvanostatic cycling experiments were performed on symmetric Na|nanocomposite|Na cells based on $NaBH_4/Al_2O_3$ and $NaNH_2/SiO_2$ prepared in the same way. After equilibration at 60 °C for at least 1 h, galvanostatic pulses were applied with a constant current density of 1.3 µA cm^{-2} for 30 min followed by a constant current density of −1.3 µA cm^{-2} for 30 min. The resulting overpotential was measured over time with either a Parstat PMC200 or Parstat PMC1000.

Solid-State NMR: To probe the interaction between the sodium salts and the oxide scaffolds, the $NaBH_4/Al_2O_3$, $NaNH_2/Al_2O_3$, and $NaNH_2/SiO_2$ nanocomposites were investigated with high-resolution solid-state nuclear magnetic resonance (ssNMR) measurements, performed on a 950 MHz Bruker NMR spectrometer equipped with a 1.3 mm triple channel (H/X/Y) CP-MAS probe at magic angle spinning (MAS) frequencies of 50 and 60 kHz. Due to frictional heating, the sample temperature was ≈50 °C. ^{11}B spectra were obtained with a 30° single pulse using ^{1}H decoupling at a 16 kHz radio frequency field strength. The ^{23}Na and ^{27}Al NMR spectra were obtained under direct polarization conditions. For reference, the ^{11}B peak in pure $NaBH_4$ was set to −42.0 ppm, in line with the literature, using $CH_3CH_2OBF_3$ as a reference ($\delta = 0$ ppm). The ^{27}Al data were referenced to a 1 M solution of $Al(NO_3)_3$ as an external standard. The ^{23}Na spectra were referenced to a 1 M solution of NaCl using $NaBH_4$ as an external standard. Prior to any measurement, sample preparation was performed in an Ar-filled glovebox, and transportation was done in air-tight holders. The NMR measurements were performed under a dry nitrogen atmosphere.

Structural Characterization: The crystalline structure of the composites was measured with X-ray diffraction (XRD) on a Bruker-AXS D8 Advance powder X-ray diffractometer using Co ($K\alpha_{1,2}$) radiation ($\lambda = 1.79026$ Å) at 30 kV and 40 mA. Diffractograms were recorded at room temperature from 20° to 85° 2θ with a 0.1° (2θ) step size and a step time of 1–3 s. Diffuse reflectance infrared Fourier transform spectroscopy (DRIFTS) measurements were performed in a Perkin–Elmer 2000 spectrometer equipped with a liquid nitrogen cooled MCT detector. Spectra were recorded between 4500 and 500 cm^{-1} with 4 cm^{-1} resolution, averaging over 16 scans, and using anhydrous KBr as a background. Differential scanning calorimetry (DSC) measurements were conducted on $NaBH_4$ nanocomposites using a TA Instruments Discovery DSC. About 6.0–8.0 mg of sample was placed in a 40 mL Al sample pan, which was closed airtight with an Al lid. The samples were cooled to −90 °C and allowed to equilibrate for 5 min. Subsequently, the samples were heated to −50 °C (1 °C min^{-1}). The measurements were performed under N$_2$ flow (50 mL min^{-1}). The phase transition temperatures were obtained from the onset of the peaks of the total heat flow, and the corresponding enthalpies were calculated from the total heat flow.

Supporting Information

Supporting Information is available from the Wiley Online Library or from the author.

Acknowledgements

Conflict of Interest

The authors declare no conflict of interest.

Data Availability Statement

The data that support the findings of this study are available from the corresponding author upon reasonable request.

Keywords

[1] B. Dunn, H. Kamath, J. M. Tarascon, *Science* **2011**, *334*, 928.
[2] J. B. Goodenough, K. S. Park, *J. Am. Chem. Soc.* **2013**, *135*, 1167.
[3] A. Mauger, C. M. Julien, *Ionics* **2017**, *23*, 1933.
[4] B. L. Ellis, L. F. Nazar, *Curr. Opin. Solid State Mater. Sci.* **2012**, *16*, 168.
[5] M. D. Slater, D. Kim, E. Lee, C. S. Johnson, *Adv. Funct. Mater.* **2013**, *23*, 947.
[6] H. Pan, Y. S. Hu, L. Chen, *Energy Environ. Sci.* **2013**, *6*, 2338.
[7] P. Adelhelm, P. Hartmann, C. L. Bender, M. Busche, C. Eufinger, J. Janek, *Beilstein J. Nanotechnol.* **2015**, *6*, 1016.
[8] C. Vaalma, D. Buchholz, M. Weil, S. Passerini, *Nat. Rev. Mater.* **2018**, *3*, 18013.
[9] J. T. Kummer, N. Weber, J. T. Kummer, N. Weber, *SAE Trans.* **1968**, *76*, 1003.
[10] X. Lu, G. Xia, J. P. Lemmon, Z. Yang, *J. Power Sources* **2010**, *195*, 2431.
[11] M. Armand, J. M. Tarascon, *Nature* **2008**, *451*, 652.
[12] J. Janek, W. G. Zeier, *Nat. Energy* **2016**, *1*, 16141.
[13] Y.-F. Y. Yao, J. T. Kummer, *J. Inorg. Nucl. Chem.* **1967**, *29*, 2453.
[14] J. B. Goodenough, H. Y. Hong, J. A. Kafalas, *Mater. Res. Bull.* **1976**, *11*, 203.
[15] H. Y. P. Hong, *Mater. Res. Bull.* **1976**, *11*, 173.
[16] M. Guin, F. Tietz, *J. Power Sources* **2015**, *273*, 1056.
[17] A. Hayashi, K. Noi, A. Sakuda, M. Tatsumisago, *Nat. Commun.* **2012**, *3*, 855.
[18] J.-J. Kim, K. Yoon, I. Park, K. Kang, *Small Methods* **2017**, *1*, 1700219.
[19] C. Zhao, L. Liu, X. Qi, Y. Lu, F. Wu, J. Zhao, Y. Yu, Y.-S. Hu, L. Chen, *Adv. Energy Mater.* **2018**, *8*, 1703012.
[20] M. Matsuo, Y. Nakamori, S. I. Orimo, H. Maekawa, H. Takamura, *Appl. Phys. Lett.* **2007**, *91*, 2.
[21] T. J. Udovic, M. Matsuo, W. S. Tang, H. Wu, V. Stavila, A. V. Soloninin, R. V. Skoryunov, O. A. Babanova, A. V. Skripov, J. J. Rush, A. Unemoto, H. Takamura, S. I. Orimo, *Adv. Mater.* **2014**, *26*, 7622.

[22] W. S. Tang, A. Unemoto, W. Zhou, V. Stavila, M. Matsuo, H. Wu, S. I. Orimo, T. J. Udovic, *Energy Environ. Sci.* **2015**, *8*, 3637.

[23] Y. Yan, J. B. Grinderslev, M. Jørgensen, L. N. Skov, J. Skibsted, T. R. Jensen, *ACS Appl. Energy Mater.* **2020**, *3*, 9264.

[24] M. Brighi, F. Murgia, R. Černý, *Cell Rep. Phys. Sci.* **2020**, *1*, 100217.

[25] S. Kim, H. Oguchi, N. Toyama, T. Sato, S. Takagi, T. Otomo, D. Arunkumar, N. Kuwata, J. Kawamura, S.-i Orimo, *Nat. Commun.* **2019**, *10*, 1081.

[26] L. Duchêne, R. S. Kühnel, D. Rentsch, A. Remhof, H. Hagemann, C. Battaglia, *Chem. Commun.* **2017**, *53*, 4195.

[27] L. Duchêne, R. S. Kühnel, E. Stilp, E. Cuervo Reyes, A. Remhof, H. Hagemann, C. Battaglia, *Energy Environ. Sci.* **2017**, *10*, 2609.

[28] R. Asakura, L. Duchêne, R. S. Kühnel, A. Remhof, H. Hagemann, C. Battaglia, *ACS Appl. Energy Mater.* **2019**, *2*, 6924.

[29] L. Duchêne, A. Remhof, H. Hagemann, C. Battaglia, *Energy Storage Mater.* **2020**, *25*, 782.

[30] M. Matsuo, H. Oguchi, T. Sato, H. Takamura, E. Tsuchida, T. Ikeshoji, S. I. Orimo, *J. Alloys Compd.* **2013**, *580*, S98.

[31] V. Gulino, M. Brighi, E. M. Dematteis, F. Murgia, C. Nervi, R. Černý, M. Baricco, *Chem. Mater.* **2019**, *31*, 5133.

[32] F. Murgia, M. Brighi, L. Piveteau, C. E. Avalos, V. Gulino, M. C. Nierstenhöfer, P. Ngene, P. E. de Jongh, R. Černý, *ACS Appl. Mater. Interfaces* **2021**, *13*, 61346.

[33] S. Breuer, V. Pregartner, S. Lunghammer, H. M. R. Wilkening, *J. Phys. Chem. C* **2019**, *123*, 5222.

[34] S. Das, P. Ngene, P. Norby, T. Vegge, P. E. de Jongh, D. Blanchard, *J. Electrochem. Soc.* **2016**, *163*, A2029.

[35] M. H. W. Verkuijlen, P. Ngene, D. W. de Kort, C. Barré, A. Nale, E. R. H. van Eck, P. J. M. van Bentum, P. E. de Jongh, A. P. M. Kentgens, *J. Phys. Chem. C* **2012**, *116*, 22169.

[36] Y. S. Choi, Y. S. Lee, K. H. Oh, Y. W. Cho, *Phys. Chem. Chem. Phys.* **2016**, *18*, 22540.

[37] Y. S. Choi, Y. S. Lee, D. J. Choi, K. H. Chae, K. H. Oh, Y. W. Cho, *J. Phys. Chem. C* **2017**, *121*, 26209.

[38] P. Ngene, P. Adelhelm, A. M. Beale, K. P. de Jong, P. E. de Jongh, *J. Phys. Chem. C* **2010**, *114*, 6163.

[39] J. Lefevr, L. Cervini, J. M. Griffin, D. Blanchard, *J. Phys. Chem. C* **2018**, *122*, 15264.

[40] D. Blanchard, A. Nale, D. Sveinbjörnsson, T. M. Eggenhuisen, M. H. W. Verkuijlen, Suwarno, T. Vegge, A. P. M. Kentgens, P. E. de Jongh, *Adv. Funct. Mater.* **2015**, *25*, 184.

[41] V. Gulino, L. Barberis, P. Ngene, M. Baricco, P. E. de Jongh, *ACS Appl. Energy Mater.* **2020**, *3*, 4941.

[42] L. M. De Kort, J. Harmel, P. E. de Jongh, P. Ngene, *J. Mater. Chem. A* **2020**, *8*, 20687.

[43] P. Ngene, S. F. H. Lambregts, D. Blanchard, T. Vegge, M. Sharma, H. Hagemann, P. E. de Jongh, *Phys. Chem. Chem. Phys.* **2019**, *21*, 22456.

[44] Y. S. Choi, Y. S. Lee, D. J. Choi, K. H. Chae, K. H. Oh, Y. W. Cho, *J. Phys. Chem. C* **2017**, *121*, 26209.

[45] N. Verdal, T. J. Udovic, J. J. Rush, X. Liu, E. H. Majzoub, J. J. Vajo, A. F. Gross, *J. Phys. Chem. C* **2013**, *117*, 17983.

[46] J. Maier, *Prog. Solid State Chem.* **1995**, *23*, 171.

[47] C. C. Liang, *J. Electrochem. Soc.* **1973**, *120*, 1289.

[48] V. Gulino, M. Brighi, F. Murgia, P. Ngene, P. de Jongh, R. Černý, M. Baricco, *ACS Appl. Energy Mater.* **2021**, *4*, 1228.

[49] X. Luo, A. Rawal, K. F. Aguey-Zinsou, *Inorganics* **2021**, *9*, 2.

[50] Y. Dou, H. A. Hansen, S. M. Xu, D. Blanchard, *Mater. Chem. Front.* **2021**, *5*, 4989.

[51] M. S. Andersson, V. Stavila, A. V. Skripov, M. Dimitrievska, M. T. Psurek, J. B. Leão, O. A. Babanova, R. V. Skoryunov, A. V. Soloninin, M. Karlsson, T. J. Udovic, *J. Phys. Chem. C* **2021**, *125*, 16689.

[52] C. F. Cheng, D. H. Park, J. Klinowski, *J. Chem. Soc. – Faraday Trans.* **1997**, *93*, 193.

[53] S. Brunauer, P. H. Emmett, E. Teller, *J. Am. Chem. Soc.* **1938**, *60*, 309.

[54] E. P. Barrett, L. G. Joyner, P. P. Halenda, *J. Am. Chem. Soc.* **1951**, *73*, 373.

[55] M. Matsuo, A. Remhof, P. Martelli, R. Caputo, M. Ernst, Y. Miura, T. Sato, H. Oguchi, H. Maekawa, H. Takamura, A. Borgschulte, A. Züttel, S. I. Orimo, *J. Am. Chem. Soc.* **2009**, *131*, 16389.

[56] R. C. Agrawal, *Indian J. Pure Appl. Phys.* **1999**, *37*, 294.

[57] Y. Filinchuk, H. Hagemann, *Eur. J. Inorg. Chem.* **2008**, *112*, 3127.

[58] K. B. Harvey, N. R. McQuaker, *Can. J. Chem.* **1971**, *49*, 3272.

[59] Y. Zhang, Q. Tian, *Int. J. Hydrogen Energy* **2011**, *36*, 9733.

[60] K. Hadjiivanov, in *Identification and Characterization of Surface Hydroxyl Groups by Infrared Spectroscopy*, 1st ed., Vol. *57*, Elsevier Inc, Amsterdam, Netherlands **2014**.

[61] J. P. O. Bohger, R. R. Eßmann, H. Jacobs, *J. Mol. Struct.* **1995**, *348*, 325.

[62] J. W. Nibler, G. C. Pimentel, *Spectrochim. Acta* **1965**, *21*, 877.

[63] S. C. Abrahams, J. Kalnajs, *J. Chem. Phys.* **1954**, *22*, 434.

[64] J. E. Olsen, P. Karen, M. H. Sørby, B. C. Hauback, *J. Alloys Compd.* **2014**, *587*, 374.

[65] C. Paterakis, S. Guo, M. Heere, Y. Liu, L. F. Contreras, M. H. Sørby, B. C. Hauback, D. Reed, D. Book, *Int. J. Hydrogen Energy* **2017**, *42*, 22538.

[66] P. E. de Jongh, T. M. Eggenhuisen, in *Nanoparticles: Workhorses of Nanoscience*, (Ed.: C. deMello Donegá), Springer, Berlin, Heidelberg **2014**, pp. 99–120.

[67] P. E. de Jongh, T. M. Eggenhuisen, *Adv. Mater.* **2013**, *25*, 6672.

[68] S. Brunauer, D. L. Kantro, C. H. Weise, *Can. J. Chem.* **1956**, *31*, 1483.

[69] M. L. Guzmán-Castillo, X. Bokhimi, A. Rodríguez-Hernández, A. Toledo-Antonio, F. Hernández-Beltrán, J. J. Fripiat, *J. Non. Cryst. Solids* **2003**, *329*, 53.

[70] Suwarno, P. Ngene, A. Nale, T. M. Eggenhuisen, M. Oschatz, J. P. Embs, A. Remhof, P. E. de Jongh, *J. Phys. Chem. C* **2017**, *121*, 4197.

[71] D. Blanchard, A. Nale, D. Sveinbjörnsson, T. M. Eggenhuisen, M. H. W. Verkuijlen, Suwarno, T. Vegge, A. P. M. Kentgens, P. E. de Jongh, *Adv. Funct. Mater.* **2015**, *25*, 184.

[72] R. J. D. Tilley, in *Defects in Solids*, John Wiley & Sons, Inc, Hoboken, NJ, USA **2008**.

[73] S. F. H. Lambregts, E. R. H. Van Eck, Suwarno, P. Ngene, P. E. de Jongh, A. P. M. Kentgens, *J. Phys. Chem. C* **2019**, *123*, 25559.

[74] V. Gulino, L. Barberis, P. Ngene, M. Baricco, P. E. de Jongh, *ACS Appl. Energy Mater.* **2020**, *3*, 4941.

[75] S. R. H. Jensen, M. Paskevicius, B. R. S. Hansen, A. S. Jakobsen, K. T. Møller, J. L. White, M. D. Allendorf, V. Stavila, J. Skibsted, T. R. Jensen, *Phys. Chem. Chem. Phys.* **2018**, *20*, 16266.

[76] E. L. Muetterties, R. E. Merrifield, H. C. Miller, W. H. Knoth, J. R. Downing, *J. Am. Chem. Soc.* **1962**, *84*, 2506.

[77] L. He, Y. Fu, D. Wu, D. Zhang, H. Cheng, H. Lin, X. Li, W. Xiong, Q. Zhu, Y. Deng, H. Shao, H. W. Li, X. Zhao, Z. Lu, *Inorganica Chim. Acta* **2018**, *474*, 16.

[78] P. Ngene, R. van den Berg, M. H. W. Verkuijlen, K. P. de Jong, P. E. de Jongh, *Energy Environ. Sci.* **2011**, *4*, 4108.

[79] C. Gautam, A. K. Yadav, A. K. Singh, *ISRN Ceram.* **2012**, *2012*, 1.

[80] E. I. Kamitsos, G. D. Chryssikos, *J. Mol. Struct.* **1991**, *247*, 1.

[81] Z. Łodziana, P. Błoński, Y. Yan, D. Rentsch, A. Remhof, *J. Phys. Chem. C* **2014**, *118*, 6594.

[82] V. Stavila, J. H. Her, W. Zhou, S. J. Hwang, C. Kim, L. A. M. Ottley, T. J. Udovic, *J. Solid State Chem.* **2010**, *183*, 1133.

[83] S. J. Hwang, R. C. Bowman, J. W. Reiter, J. Rijssenbeek, G. L. Soloveichik, J. C. Zhao, H. Kabbour, C. C. Ahn, *J. Phys. Chem. C* **2008**, *112*, 3164.

[84] L. Züchner, J. C. C. Chan, W. Müller-Warmuth, H. Eckert, *J. Phys. Chem. B* **1998**, *102*, 4495.

**ADVANCED
SCIENCE NEWS**

www.advancedsciencenews.com

**ADVANCED
FUNCTIONAL
MATERIALS**

www.afm-journal.de

[85] A. Düvel, E. Romanova, M. Sharifi, D. Freude, M. Wark, P. Heitjans, M. Wilkening, *J. Phys. Chem. C* **2011**, *115*, 22770.

[86] R. Zettl, M. Gombotz, D. Clarkson, S. G. Greenbaum, P. Ngene, P. E. de Jongh, H. M. R. Wilkening, *ACS Appl. Mater. Interfaces* **2020**, *12*, 38570.

[87] M. Choi, K. Matsunaga, F. Oba, I. Tanaka, *J. Phys. Chem. C* **2009**, *113*, 3869.

[88] V. Epp, M. Wilkening, *ChemPhysChem* **2013**, *14*, 3706.

[89] R. M. Bota, K. Houthoofd, P. J. Grobet, P. A. Jacobs, K. U. Leuven, *Catal. Today* **2010**, *152*, 99.

[90] K. Shimoda, Y. Zhang, T. Ichikawa, H. Miyaoka, Y. Kojima, *J. Mater. Chem.* **2011**, *21*, 2609.

[91] J. Shen, M. Tu, C. Hu, Y. Cheni, *Langmuir* **1998**, *14*, 2756.

[92] F. Deng, Y. Du, C. Ye, Y. Kong, *Solid State Nucl. Magn. Reson.* **1993**, *2*, 317.

[93] S. Xin, Q. Wang, J. Xu, N. Feng, W. Li, F. Deng, *Solid State Nucl. Magn. Reson.* **2017**, *84*, 103.

[94] K. I. Hadjiivanov, *Catal. Rev. – Sci. Eng.* **2000**, *42*, 71.

[95] K. Hadjiivanov, V. Bushev, M. Kantcheva, D. Klissurski, *Langmuir* **1994**, *10*, 464.

[96] J. Coates, in *Encyclopedia of Analytical Chemistry*, John Wiley & Sons Ltd, Chichester, UK **2006**, pp. 196–199.

[97] A. Boukaoud, Y. Chiba, D. Sebbar, *Vib. Spectrosc.* **2021**, *116*, 103280.

[98] M. Piumetti, M. Armandi, E. Garrone, B. Bonelli, *Microporous Mesoporous Mater.* **2012**, *164*, 111.

[99] E. H. Teunissen, R. A. Van Santen, A. P. J. Jansen, F. B. van Duijneveldt, *J. Phys. Chem.* **1993**, *97*, 203.

[100] A. R. Jones, R. Winter, G. N. Greaves, I. H. Smith, *J. Phys. Chem. B* **2005**, *109*, 23154.

[101] X. Xue, J. Stebbins, *Phys. Chem. Miner.* **1993**, *20*, 297.

[102] H. Koller, G. Engelhardt, A. P. M. Kentgens, J. Sauer, *J. Phys. Chem.* **1994**, *98*, 1544.

[103] I. Chorkendorff, J. W. Niemantsverdriet, in *Concepts of Modern Catalysis and Kinetics*, 2nd ed., John Wiley & Sons, Weinheim **2003**.

[104] H. J. Lin, P. Zhang, Y. X. Fang, Y. J. Zhao, H. Zhong, J. J. Tang, *J. Phys. Chem. C* **2019**, *123*, 18180.

[105] P. Martelli, R. Caputo, A. Remhof, P. Mauron, A. Borgschulte, A. Žttel, *J. Phys. Chem. C* **2010**, *114*, 7173.

[106] J. Urgnani, F. J. Torres, M. Palumbo, M. Baricco, *Int. J. Hydrogen Energy* **2008**, *33*, 3111.